

Contents lists available at ScienceDirect

Intermetallics

journal homepage: www.elsevier.com/locate/intermet





Low cycle fatigue performances of $Al_{0.3}$ CoCrFeNi high entropy alloys: In situ neutron diffraction studies on the precipitation effects

Zongyang Lyu^a, Chuhao Liu^b, Di Xie^a, Rui Feng^c, Dunji Yu^c, Yan Chen^c, Ke An^c, Yanfei Gao^{a,*}, Huamiao Wang^{b,**}, Peter K. Liaw^{a,***}

- ^a Department of Materials Science and Engineering, University of Tennessee, Knoxville, TN, 37996, USA
- ^b School of Mechanical Engineering, Shanghai Jiaotong University, Shanghai, 200240, China
- ^c Neutron Scattering Division, Oak Ridge National Laboratory, Oak Ridge, TN, 37831, USA

ARTICLE INFO

Keywords: High-entropy alloy In situ neutron diffraction Low-cycle fatigue Elastic-viscoplastic self-consistent model

ABSTRACT

Fatigue properties are essential for structural materials in industrial applications. High-entropy alloys are promising fatigue-resistant alloys with high strengths and good ductilities. In this study, the B2 precipitate significantly increased the yield strength of the $Al_{0.3}$ CoCrFeNi high-entropy alloy but at the same time decreased the low-cycle fatigue life. A detailed investigation of the underlying mechanisms will provide critical insights into the precipitate effect on the fatigue performance of high-entropy alloys. Here, the $Al_{0.3}$ CoCrFeNi alloys with single face-centered-cubic (FCC) phase and with FCC + B2 phases are used for the investigation of the low-cycle fatigue behavior by combining in situ neutron diffraction measurements and elastic-viscoplastic self-consistent modeling. The simulation results indicate that the B2 precipitates highly increased the back stresses during cyclic loading by facilitating the kinematic hardening in the matrix, while the effect of dynamic recovery is relatively weak. The increase in back stresses provides more fatigue-crack-initiation sites and thus the damage accumulation, which will further lead to a shorter fatigue life.

1. Introduction

High-entropy alloys (HEAs), also called multicomponent alloys, is a newly developed alloying strategy. Unlike the traditional alloys with one or two principal elements, HEAs have five principal elements and simple main phase structures, such as face-centered-cubic (FCC), bodycentered-cubic (BCC), and hexagonal-close-packed (HCP) [1–3]. HEAs have demonstrated excellent mechanical properties including strength, ductility, and fracture toughness [2,4–12]. However, most of the studies on HEAs are focused on the monotonic tension or compression tests [1–7]. The understanding of fatigue behaviors of HEAs is still limited, especially for low-cycle fatigue (LCF). The most well-known HEA (Cantor alloy), CoCrFeMnNi, has been investigated for the LCF property [13–17]. The CoCrFeMnNi alloy with single FCC phase has similar fatigue-crack growth behavior to twinning-induced plasticity (TWIP) steel and the LCF life of CoCrFeMnNi is lower than that of TWIP steel at all strain amplitudes (0.85%–0.3%), but higher than that of SS304 steel

at high strain amplitudes (0.85%-0.55%) [14]. Even though the LCF life is higher than that of SS304 steel at high strain amplitudes, the strength is still lower than that of other high-strength materials. Equal Channel Angular Pressing (ECAP) was conducted to increase the yield strength of the Cantor alloy by Picak et al. [13], and the cyclic response of both coarse-grained and ultrafine-grained Cantor alloys was investigated during LCF at room temperature. The ECAP sample exhibits greater fatigue life (~80000 cycles) at the strain amplitude of 0.2% than the hot-extruded (HE) sample (\sim 37000 cycles). The HE sample has a better fatigue life (~3000 cycles) at the strain amplitude of 0.6% than the ECAP sample (~1100 cycles) [13]. However, the high-Mn austenitic alloy, FeMn₃₀ has a higher LCF life (~10000 cycles) than the HE and ECAP CoCrFeMnNi samples at the strain amplitude of 0.6%. The grain-size effect on LCF of a carbon-containing CoCrFeMnNi HEA was investigated by Shams et al. [15], and the fatigue life of warm-rolled and annealed samples with small grain sizes was increased at low total strain amplitudes (0.4% and 0.55%), which is attributed to an increase in the

E-mail addresses: ygao7@utk.edu (Y. Gao), wanghm02@sjtu.edu.cn (H. Wang), pliaw@utk.edu (P.K. Liaw).

^{*} Corresponding author.

^{**} Corresponding author.

^{***} Corresponding author.

elastic resistance owing to the higher strength of the fine-grained HEA than the coarse-grained HEA. Besides the investigations on the FCC Cantor alloy, the BCC HfNbTiZr refractory HEA [18], multi-phase non-equiatomic FeCrNiMnCo HEA [19], precipitate strengthened Al0.5CoCrFeNi [20] and Al0.5CoCrFeMnNi [21] HEAs, and metastable HEAs [22-24] have been studied for the low-cycle fatigue behaviors. It is worth mentioning that the ductile-transformable multicomponent B2 precipitates were proven to enhance both the strength and the low-cycle fatigue life of the Al_{0.5}CoCrFeNi HEA by Feng et al. [20]. They found that the Al_{0.5}CoCrFeNi HEA with a ductile-transformable multicomponent B2 exhibits at least four times longer life than conventional alloys at the plastic strain amplitude of $\sim\!0.03\%$ and maintains comparable LCF properties with traditional alloys at high strain levels. The fine ductile-transformable B2 phase could hinder the initiation of microcracks because of stress relaxation and strain partitioning during plastic deformation and martensitic transformation, which facilitate the relief of cyclic damage accumulation caused by the deformation incompatibility between the B2 and FCC phases [20]. In this case, the precipitate can enhance both the strength and LCF resistance. In addition, some research showed that the coherent precipitates in aluminum alloys are easily cut by dislocations and consequently lead to slip localization and early failure [25]. For alloys with two phases, the back stress generated from the "phase to phase" strain incompatibility, plastic strain incompatibilities, and heterogeneous plastic deformation could play an important role in the cyclic response during cyclic loading, such as the Ti-6Al-4V alloy [26].

In the present work, we investigated the LCF behavior of the $Al_{0.3}$ CoCrFeNi high-entropy alloy (denoted as $Al_{0.3}$), and the $Al_{0.3}$ with a single FCC phase has excellent LCF life at high strain amplitudes (>1%). The $Al_{0.3}$ with an FCC + B2 phase structure has also been studied for comparison. With the B2 precipitate strengthening, the yield strength of $Al_{0.3}$ nearly doubles while the LCF life becomes shorter. The combination of in situ neutron diffraction and elastic-viscoplastic self-consistent (EVPSC) modeling is used in this work to study the LCF behavior of the $Al_{0.3}$ CoCrFeNi HEA. The deformation behaviors, such as lattice-strain evolutions, of different grain families of phases along the loading direction could be measured by the in-situ neutron diffraction, which provides the input information for the EVPSC model simulations. The present research could assist us to have a better understanding of the incoherent precipitate effect on the FCC HEAs during LCF.

2. Experimental procedures

2.1. Material processing

The Al $_{0.3}$ CoCrFeNi HEA was fabricated by melting pure elements with a purity higher than 99.9 wt percent (wt. %) and casting into a plate. Then the plate was treated using hot-isostatic pressing (HIP) at 1204 °C and 103 MPa for 4 h in the air to reduce the casting defects. After that, there were two different heat treatments for the Al $_{0.3}$ CoCrFeNi HEA in air. One was the homogenization at 1200 °C for 1 h, followed by water quenching for a single FCC alloy. Another was annealed at 700 °C for 500 h after the 1200 °C homogenization, followed by water quenching, for the FCC + B2 phase alloy.

2.2. Mechanical testing

The dog-bone samples with gauge dimensions of $\phi 8mm \times 16$ mm were used for the low-cycle fatigue (LCF) test. The strain-controlled LCF tests were performed on both single FCC and FCC + B2 alloys at room-temperature using an MTS Model 810 servo-hydraulic machine with the strain rate of $1\times 10^{-2}~s^{-1}$ in air and the initial loading was in tension. The strain amplitudes were $\pm 0.25\%,~\pm 0.35\%,~\pm 0.5\%,~\pm 1.0\%,$

 $\pm 1.25\%$, and $\pm 1.5\%$ for each alloy.

2.3. Microstructural characterizations

The microstructure was characterized by a Zeiss EVO scanning-electron microscope (SEM). The specimens for SEM were initially polished with the 1200-grit SiC paper and then performed vibratory polishing with the 0.05 μm SiC suspension for the final surface. The transmission electron microscope (TEM) was performed on a ZEISS LIBRA 200 HT FE MC. The TEM samples were prepared by twin-jet polishing with an electrolyte consisting of 95% ethanol and 5% perchloric acid in a volume fraction under $-40\,^{\circ}\text{C}$ and a voltage of 30 V.

2.4. In situ neutron diffraction measurement

The in situ LCF neutron-diffraction test was performed, using an MTS load frame at the VULCAN Engineering Materials Diffractometer [27, 28], the Spallation Neutron Source (SNS), Oak Ridge National Laboratory (ORNL). The fully-reversed strain-controlled LCF tests were conducted at different strain amplitudes with triangular loading waveforms under a continuous-loading condition. The strain amplitude was $\pm 1\%$, and the initial loading is in tension. The diffraction data were recorded with a strain rate of $\sim 7\times 10^{-6}~\text{s}^{-1}$. The data of LCF were collected at several selected cycles based on the lab results, such as 1st, 2nd, and 5th cycles. The in situ neutron diffraction data were analyzed, using the VULCAN Data Reduction and Interactive Visualization software (VDRIVE) [29]. The lattice strain of a given (hkl) plane is determined by:

$$\varepsilon_{hkl} = \frac{d_{hkl} - d_{hkl}^0}{d_{hkl}^0} \tag{1}$$

where d_{hkl}^0 and d_{hkl} refer to lattice d-spacing in the stress-free condition and the lattice d-spacing during the loading condition, respectively.

2.5. Elastic visco-plastic self-consistent simulations

The collective deformation behavior of polycrystalline aggregates was nicely modeled by the EVPSC model [20]. As for an individual grain, the total strain rate can be expressed as:

$$\dot{\boldsymbol{\varepsilon}} = \dot{\boldsymbol{\varepsilon}}^e + \dot{\boldsymbol{\varepsilon}}^p = \boldsymbol{M}^e : \dot{\boldsymbol{\sigma}} + \boldsymbol{M}^p : \boldsymbol{\sigma} + \dot{\boldsymbol{\varepsilon}}_0$$
 (2)

where $\dot{\varepsilon}^e$ and $\dot{\varepsilon}^p$ stand for the elastic strain rate and plastic strain rate, respectively. M^e , M^p , and $\dot{\varepsilon}_0$ represent the elastic compliance, plastic compliance, and back-extrapolated strain rate, respectively. The macroscope strain rate has a the similar formula and can be written as the following equation [30]:

$$\dot{E} = \overline{M}^e : \dot{\Sigma} + \overline{M}^p : \Sigma + \dot{E}_0 \tag{3}$$

where \overline{M}^e , \overline{M}^p , and \dot{E}_0 are the elastic compliance, plastic compliance, and back-extrapolated strain rate for a homogeneous effective medium, respectively. An extended Voce law is applied to simulate the work-hardening behavior of the slip systems, as expressed by Ref. [30]:

$$\widehat{\tau}_{cr} = \tau_0 + (\tau_1 + h_1 \Gamma) \left\{ 1 - \exp\left(-\frac{h_0 \Gamma}{\tau_1}\right) \right\} \tag{4}$$

where τ_0 , h_0 , h_1 , and $\tau_0 + \tau_1$ stand for the initial critical resolved shear stress, initial hardening rate, asymptotic hardening rate, and back-extrapolated critical resolved shear stress, respectively. Besides, $\Gamma = \int \sum_a |\dot{\gamma}^a| dt$ refers to the accumulated shear strain. In addition, the effect of the neighbor grain's deformation system, β , on the current grain's deformation system, α , is also considered by introducing the latent-hardening parameter, $h^{\alpha\beta}$, which is expressed below [30]:

$$\dot{\tau}_c^{\alpha} = \frac{d\hat{\tau}_{cr}}{d\Gamma} \sum_{\beta} h^{\alpha\beta} \dot{\gamma}^{\beta} \tag{5}$$

where $\dot{\gamma}^{\beta}$ represents the shear rate of β , and $\dot{\tau}^{\alpha}_{c}$ is the rate of the critical resolved shear stress (CRSS). Thus, the shear-strain evolution in the deformation system, α , of a specific individual grain can be written as [201:

$$\dot{\gamma}^{\alpha} = \dot{\gamma}_0 \left| \frac{\tau^{\alpha} - \tau_b^{\alpha}}{\tau^{\alpha}} \right|^{\frac{1}{m}} sgn(\tau^{\alpha} - \tau_b^{\alpha})$$
 (6)

where $\dot{\gamma}_0$, τ^α , and m denote the reference value of the shear rate, resolved shear stress (RSS), and rate-sensitive exponent, respectively. By solving the microscopic deformation behavior of an individual grain and its interaction with the overall equivalent aggregate composed of all grains, the macro and micro mechanical response of the material can be simulated separately and make connections between the finite plastic deformation modes with macroscope mechanical properties. What's more, the evolution of the back stress in a specific deformation system, α , is also involved in our model for the purpose of explaining the Bauschinger effect in cycle loading:

$$\dot{\tau}_{b}^{a} = \xi^{a} sgn(\dot{\gamma}^{a}) \sum_{\beta} q^{a\beta} |\dot{\gamma}^{\beta}| - \eta^{a} \tau_{b}^{a} \sum_{\beta} q^{a\beta} |\dot{\gamma}^{\beta}|$$
 (7)

where the first term is the linear kinematic hardening, and the second term is the dynamic recovery. ξ and η are the corresponding coefficients of the two terms.

3. Results

3.1. Microstructures of undeformed AlO.3 HEAs

The microstructures of the Al0.3 HEA samples by SEM are shown in Fig. 1(a) and (b). As shown in Fig. 1(a), the Al0.3 HEA with a single FCC phase had a homogeneous microstructure. The microstructure of the Al0.3 HEA with an FCC matrix and B2 precipitates is shown in Fig. 1(b). The needle-like B2 precipitates with a length of less than 2 μm were uniformly distributed in the FCC matrix. The neutron diffraction patterns of the single FCC and FCC + B2 samples are exhibited in Fig. 1(c) and (d), respectively, which are consistent with the SEM results. The B2 precipitates were incoherent and the lattice constants of the FCC matrix and B2 precipitate were $\sim 3.582 \ \mbox{\normalfont{A}}$ and $\sim 2.866 \ \mbox{\normalfont{A}}$, respectively, based on the neutron diffraction measurement.

3.2. Low-cycle behavior of the Al0.3 HEAs

The initial tension part and hysteresis loops (stress vs. strain) of the Al0.3 HEA samples under LCF with the strain amplitude of $\pm 1\%$ are shown in Fig. 2. In Fig. 2(a) and (b), the hysteresis loops of the 1st cycle were symmetric in the Al0.3 HEAs with and without B2 precipitate. The yield strength of the FCC Al0.3 HEA was ~170 MPa, and the maximum stress at the strain of 1% was \sim 210 MPa, as presented in Fig. 2(a). The yield strength and maximum stress of the FCC + B2 Al0.3 HEA were ~350 MPa and 420 MPa, respectively, given in Fig. 2(b). The initial tension part of the Al0.3 HEA with the B2 precipitate showed work hardening while that of the Al0.3 with a single FCC phase had relatively low hardening behavior. An obvious increase of the maximum stress can be observed in the cyclic tensile stage, compared with the initial tension in both alloys. This trend indicates that the cyclic hardening occurred during the LCF of the Al0.3 at the strain amplitude of $\pm 1\%$. It is worth mentioning that there were unexpected serrated flows on the plastic region of all the hysteresis loops, although the serrated flow usually occurred under the condition of high or cryogenic temperature and low strain rate ($\sim 10^{-3}$ or 10^{-4} s⁻¹) [31–39]. The hysteresis loops of different cycles are shown in Fig. 2(c) and (d) for the Al0.3 HEAs with an FCC phase and FCC + B2 phases, respectively. The increasing maximum stress of the single FCC sample until the 100th cycle indicates an obvious cyclic hardening during LCF. After the 100th cycle, the maximum stresses tended to stay at the same level. On the other hand, the hysteresis loops of the FCC + B2 sample showed a very similar shape without obvious cyclic hardening.

The comparison of the relationship of the total strain amplitude versus the reversals to failure $(2N_f)$ for different alloys is shown in Fig. 3 (a), including the present Al0.3 HEA, other representative HEAs and conventional alloys [13,20,26,40-42]. The studied Al0.3 HEAs showed comparable LCF properties with the conventional alloys and other HEAs. Fig. 3(b) shows the relationship of the total strain amplitude as a function of the reversals to failure $(2N_f)$. The Al0.3 HEA with a single FCC phase had a slightly higher LCF life than the Al0.3 HEA with B2 precipitates. The Basquin and Coffin-Manson laws were combined for predicting the LCF life because it contains both the elastic and plastic regions. The Basquin law [43] described as:

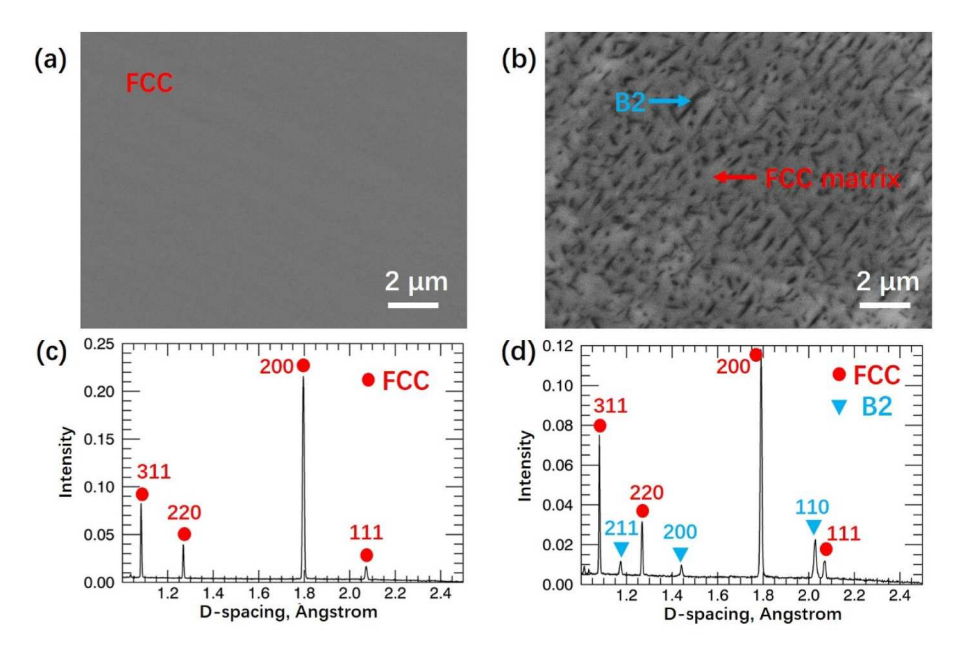


Fig. 1. The microstructures of the $Al_{0.3}$ CoCrFeNi HEAs (a) with a single FCC phase and (b) with FCC + B2 phases by SEM and neutron diffraction patterns of the single FCC (c) and FCC + B2 (d) samples.

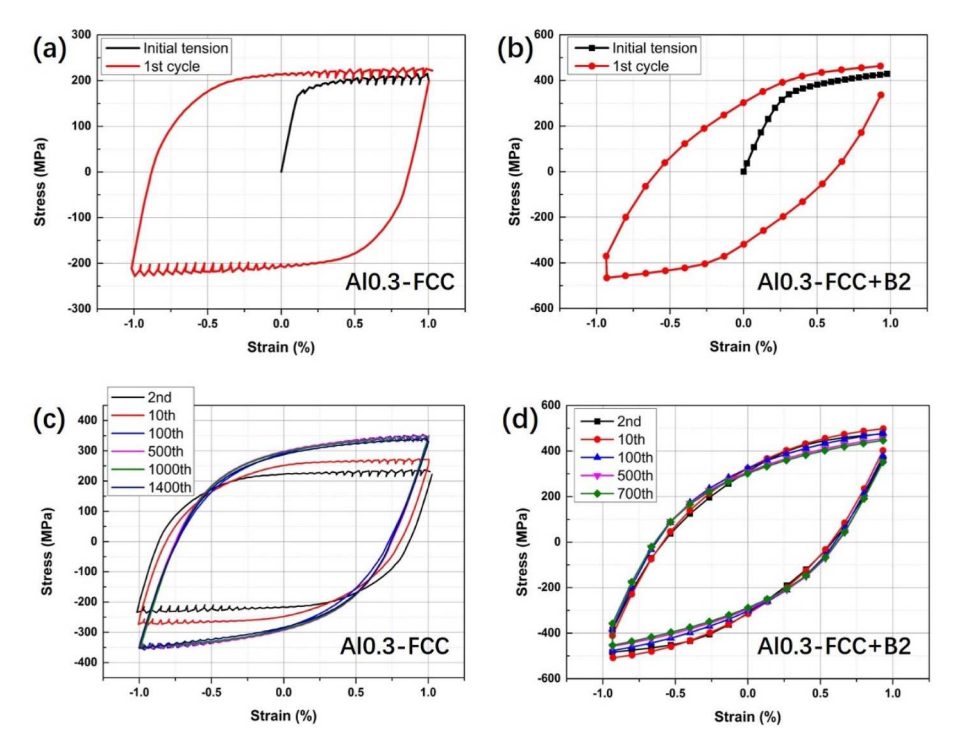


Fig. 2. The initial tension and hysteresis loops of the $Al_{0.3}$ CoCrFeNi HEA (a)(c) with a single FCC phase and (b)(d) with FCC + B2 phases at the strain amplitude of 1%.

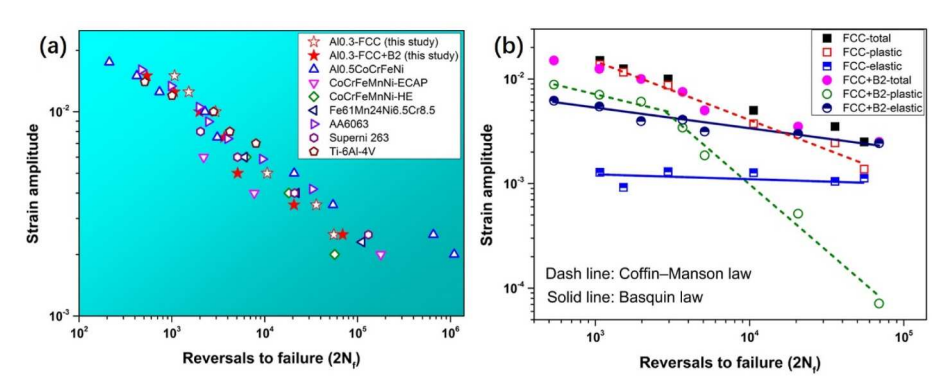


Fig. 3. (a) The comparison of low cycle fatigue data for the present alloy, other HEAs, and conventional alloys [13,16,18,32–34]; (b) The total strain amplitude, plastic strain amplitude, and elastic strain amplitude vs. the number of reversals to failure for the Al_{0.3}CoCrFeNi HEA HEAs with a single FCC phase and with FCC + B2 phases, which are used for Coffin-Manson & Basquin analyses.

$$\frac{\Delta \sigma}{2} = \sigma_f' \left(2N_f \right)^b \tag{8}$$

where $\Delta \sigma$ is the total stress amplitude; σ_f' is the fatigue-strength coefficient; N_f is the number of cycles to failure; b is the fatigue-strength exponent. The Coffin-Manson law [44,45] is given by the following equation:

$$\frac{\Delta \varepsilon_p}{2} = \varepsilon_f' (2N_f)^c \tag{9}$$

where $\frac{\Delta \varepsilon_p}{2}$ is the plastic-strain amplitude; N_f is the number of cycles to failure; ε_f' is the fatigue-strain coefficient; and c is the fatigue-ductility exponent. Based on the two equations above, the total fatigue-life prediction can be expressed as:

$$\frac{\Delta \varepsilon}{2} = \frac{\Delta \varepsilon_e}{2} + \frac{\Delta \varepsilon_p}{2} = \frac{\sigma_f'}{E} (2N_f)^b + \varepsilon_f' (2N_f)^c$$
(10)

where $\frac{\Delta \varepsilon}{2}$ is the total strain amplitude; $\frac{\Delta \varepsilon_e}{2}$ is the elastic-strain amplitude; $\frac{\Delta \varepsilon_p}{2}$ is the plastic-strain amplitude; σ_f is the fatigue-strength coefficient; E is the elastic modulus; N_f is the number of cycles to failure; b is the fatigue-strength exponent; ε_f is the fatigue-strain coefficient; and c is the fatigue-ductility exponent. The fitting parameters for the Basquin and Coffin-Manson laws in the Al0.3 are shown in Table 2 HEA and the elastic modulus of FCC and FCC + B2 sample were 142.8 GPa and 186.3 GPa, respectively, calculated from the initial tensile part.

3.3. Low-cycle fatigue behavior by in situ neutron diffraction

The lattice-strain evolutions of different grain families of the Al0.3 HEAs along the loading direction during LCF are shown in Fig. 4. The lattice-strain evolutions are related to specific deformation mechanisms [46,47]. The lattice-strain evolutions of the $\{200\}$, $\{220\}$, and $\{331\}$ grain families of the FCC Al0.3 along the loading direction during initial tension are exhibited in Fig. 4(a). The lattice strains in the initial tension

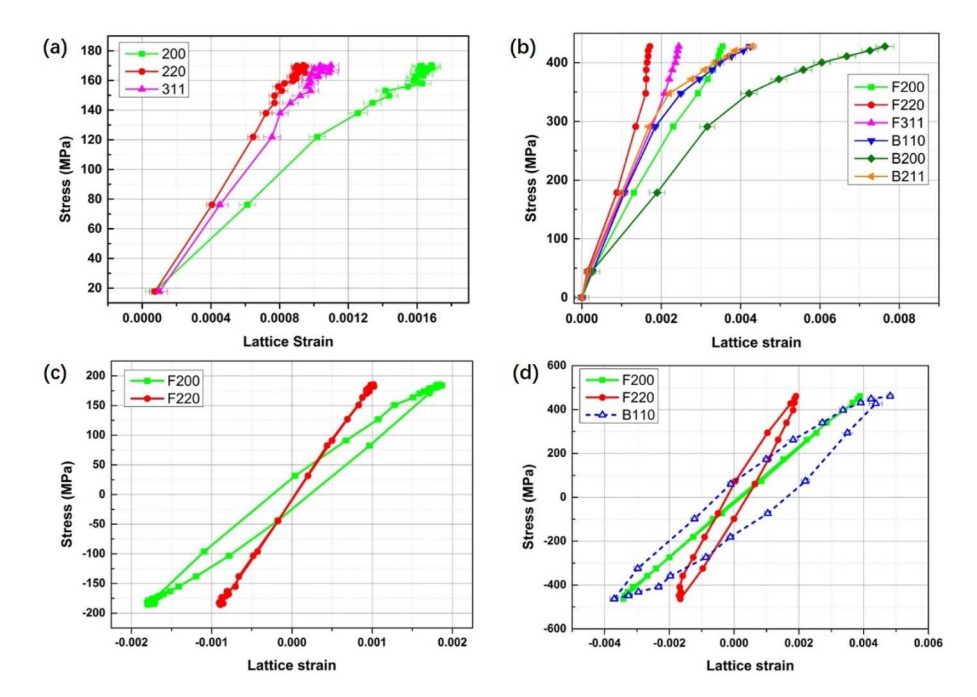


Fig. 4. The lattice-strain evolutions along the loading direction of the $Al_{0.3}$ CoCrFeNi HEA (a)(c) with a single FCC phase and (b)(d) with FCC + B2 phases at the strain amplitude of 1%. (a)(b) are the initial tension part and (c)(d) are the 1st cycle.

of the FCC Al0.3 increased linearly with the applied stress. The first vertical inflection of the lattice strain was observed at ~123 MPa in {311} and {220} grain orientations, while the inflection in {200} was horizontal. This feature indicates that the {200} grain family along the loading direction tended to share more load during the tensile deformation. The third vertical inflection was at the stress of \sim 158 MPa in the {200} grain family. This trend suggests the macro yielding of this alloy was strongly associated with the inflection point of the {200} grain family. Fig. 4(b) presents the lattice-strain evolutions of {200}, {220}, and {311} grain families of the FCC phase and {110},{200}, and {211} grains of the B2 phase in the FCC + B2 Al0.3 HEA during initial tension. The lattice strains of grain families of FCC (200) and FCC (311) turned upward firstly at ~350 MPa while others have horizontal inflections. The FCC $\{220\}$ had its first upward trend at ~ 370 MPa. The macro yielding of Al0.3 HEA with B2 precipitates was associated with the yielding point of the FCC {200} which is also observed in the single FCC Alo.3 HEA. The grain families of B2 phase shared more load than the FCC phase, especially the B2 {200} grain orientation.

In Fig. 4(c) and (d), the lattice-strain evolutions of different grain families of the Al0.3 HEAs along the loading direction during the 1st LCF cycle are plotted. The lattice strain hysteresis loops were symmetric in the two alloys. The lattice-strain evolutions in the reverse compression and following tension parts were similar to the initial tension. In the Alo.3 with a single FCC phase, shown in Fig. 4(c), the FCC {220} grain family had an almost linear trend compared to the FCC {200}. Because the FCC {200} took more load sharing during the deformation than the FCC {220} in the single FCC phase sample. It can be seen clearly in Fig. 4 (a) that the lattice strain of FCC {200} had an obvious right turn in the late stage of tensile part. For the Al0.3 with B2 precipitates, instead of FCC {220}, the FCC {200} grain family had no obvious lattice-strain loop while B2 {110} takes the largest loop, as presented in Fig. 4(d). For the FCC + B2 sample, the B2 {110} took more load sharing than the grain families of FCC phase during the deformation. The B2 {110} had the right turn in the late stage of tensile part and the lattice strain evolution formed a hysteresis loop in clockwise direction under cyclic loading. On the other hand, both the FCC {200} and FCC {220} turned upwards in the late stage of tensile part and the FCC {220} turned earlier than the FCC {200}. In this case, the FCC {220} showed a much larger

hysteresis loop, which is in anticlockwise direction, than the FCC $\{200\}$. The hysteresis loop of FCC $\{200\}$ is too small compared with FCC $\{220\}$ and B2 $\{110\}$ and it makes the FCC $\{200\}$ show an almost linear trend in FCC + B2 sample during cyclic loading.

3.4. Microstructures of deformed Al0.3 HEAs after LCF

The fracture surface of the failed Al0.3 with a single FCC phase after LCF with the strain amplitude of $\pm 1\%$ is shown in Fig. 5(a) and (b). As shown in Fig. 5(a), the crack initiated at the surface and propagated into the sample. In Fig. 5(b), the striations near the crack-initiation site show a stable crack-growth region, which indicates the transgranular ductile fracture feature. There were secondary cracks accompanying the striations near the crack initiation, which will influence the crack-propagation process to a certain extent.

The dislocation structures of the Al0.3 samples after LCF with a strain amplitude of 1% are shown in Fig. 6. A high density of interacting dislocations and dislocation forests can be observed in the Al0.3 with a single FCC phase as shown in Fig. 6(a). For the Al0.3 with B2 precipitates, as shown in Fig. 6(b), the dislocations are mostly gathered around the B2 precipitates which are pointed by the red arrows. It indicates that the B2 precipitates acted as obstacles and hindered the movements of dislocations. The strain incompatibility between the FCC and B2 phase contributed to the dislocation pile-ups around the phase boundaries of B2. In the meantime, these dislocation pile-ups will increase the plastic heterogeneity between the FCC and B2 phases, which leads to an increase in the back stresses during cyclic loading. The main deformation mechanism in the Al0.3 samples is the dislocation slip. No twinning was found in the failed Al0.3 samples after LCF with the strain amplitude of $\pm 1\%$.

4. Discussions

According to the TEM results, the initial strain hardening of the Al0.3 under LCF with the strain amplitude of $\pm 1\%$ was attributed to the dislocation generation and interactions. The evolution of the dislocation density was investigated, using the proportional relationship between dislocation density and full width at half maximum (FWHM) [20,48,49].

Fig. 5. The SEM results of the fracture surfaces of the FCC $Al_{0.3}$ CoCrFeNi HEA after LCF (a) crack initiation; (b) striations and secondary cracks near the crack-initiation site.

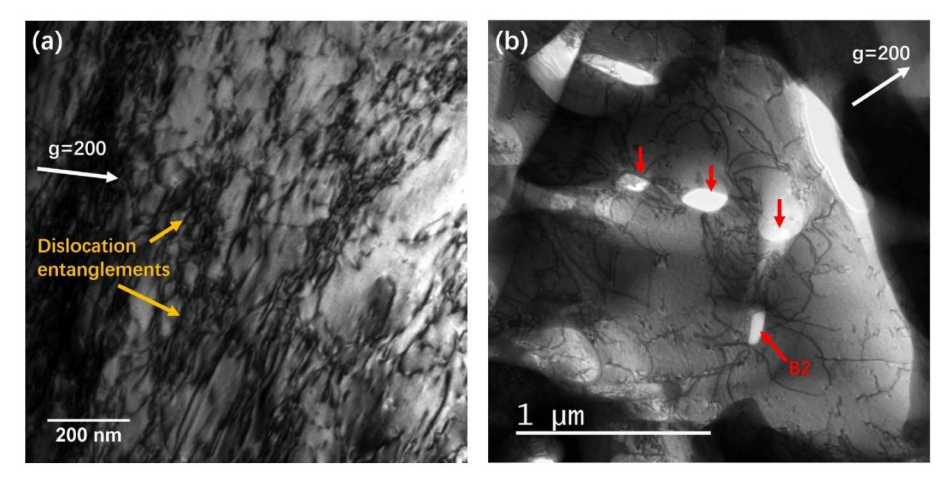


Fig. 6. The TEM images of dislocation structures in the $Al_{0.3}$ CoCrFeNi HEA with a single FCC phase in (a) and FCC + B2 phases in (b) along the [110] zone axis after LCF with the strain amplitude of 1%.

In this way, we can use the evolution of FWHM to illustrate the evolution of dislocation density. Fig. 7(a) shows the FWHM evolution of the FCC $\{200\}$ and $\{220\}$ in the FCC Alo.3 HEA from the initial tension to the 2nd cycle with a strain amplitude of 1%. All the FWHM values of the grain families had an increasing trend during the initial tension to the strain of 1%. In the reverse compression part, the FWHM decreased to a valley point at the strain of \sim 0%, i.e., a load-free condition, and

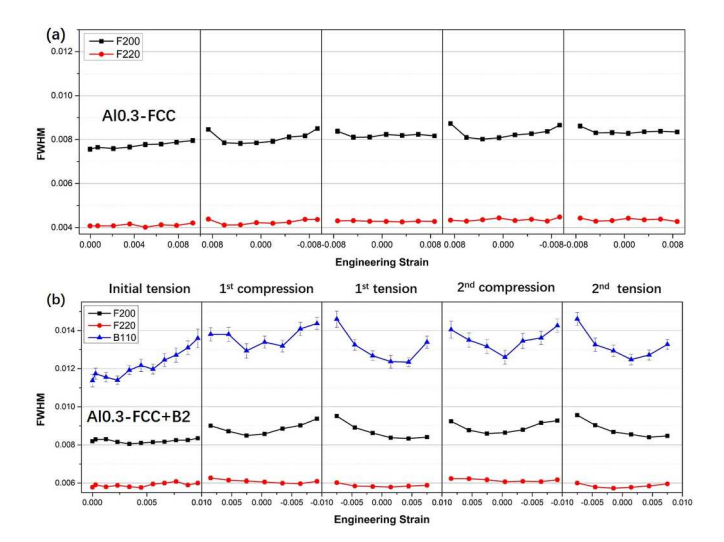


Fig. 7. The FWHM vs. applied engineering strain of the ${\rm Al_{0.3}CoCrFeNi}$ HEA (a) with a single FCC phase and (b) with FCC + B2 phases at the strain amplitude of 1%.

increased again the strain reached -1%.Similar as decreasing-valley-increasing of FWHM can be observed in the following tensile and compressive stages. The FWHM values at the strain \sim 0%, i. e., a load-free condition, could be used to illustrate the accumulation of dislocations because there is a minimum influence of the applied load at this point. The FWHM vs. applied engineering strain of the FCC {200}, FCC {220}, and B2 {110} in the FCC + B2 Al0.3 HEA is exhibited in Fig. 7(b). The FWHM values of the B2 and FCC phases showed a similar evolution trend as those in the single FCC sample during cyclic loading. The dislocation density periodically reached valley positions accompanied by stress-free conditions during LCF and the overall values were slightly increased due to the dislocation accumulations at phase boundaries.

Predictions from the EVPSC model are given by the overall stressstrain cycles in Fig. 8, and the lattice strain evolutions in single phase HEA and two-phase HEA in Figs. 9 and 10, respectively. The calibration of constitutive parameters in Section 2.5 is discussed below. First, elastic constants can be accurately obtained from fitting to the lattice strain data in the initial tensile loading stage. Second, when plastic deformation occurs, lattice strain curves display the "splitting" behavior. Again in the first loading step, the hard grain families will lead to the rightward splitting while the soft grain families will correspond to the upward splitting. Using the yield sequence of such grain families and their subsequent relative slopes, we can determine both the slip systems and the hardening parameters. In Al0.3 HEA, the dominant plasticdeformation mode is the $\{111\}\langle 1\overline{1}0\rangle$ dislocation-slip system, which is very common in the FCC structure of Al_xCoCrFeNi when the Al content is less than 7% [20]. Fitting to the neutron data in Figs. 9(a) and Fig. 10, the plastic-deformation and work-hardening behaviors are confirmed to be $\{111\}\langle 1\overline{1}0\rangle$ slip in FCC phase and $\{110\}\langle 001\rangle$ slip in B2 phase, and

Z. Lyu et al. Intermetallics 168 (2024) 108241

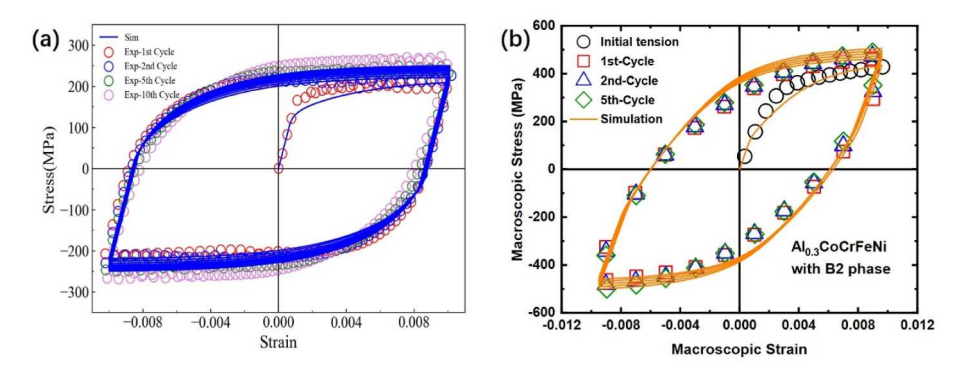


Fig. 8. (a) True stress-strain curves and (b) cyclic response of the initial tension and the first ten cycles of experiment with the corresponding EVPSC simulation results of the FCC $Al_{0.3}$ CoCrFeNi HEA.

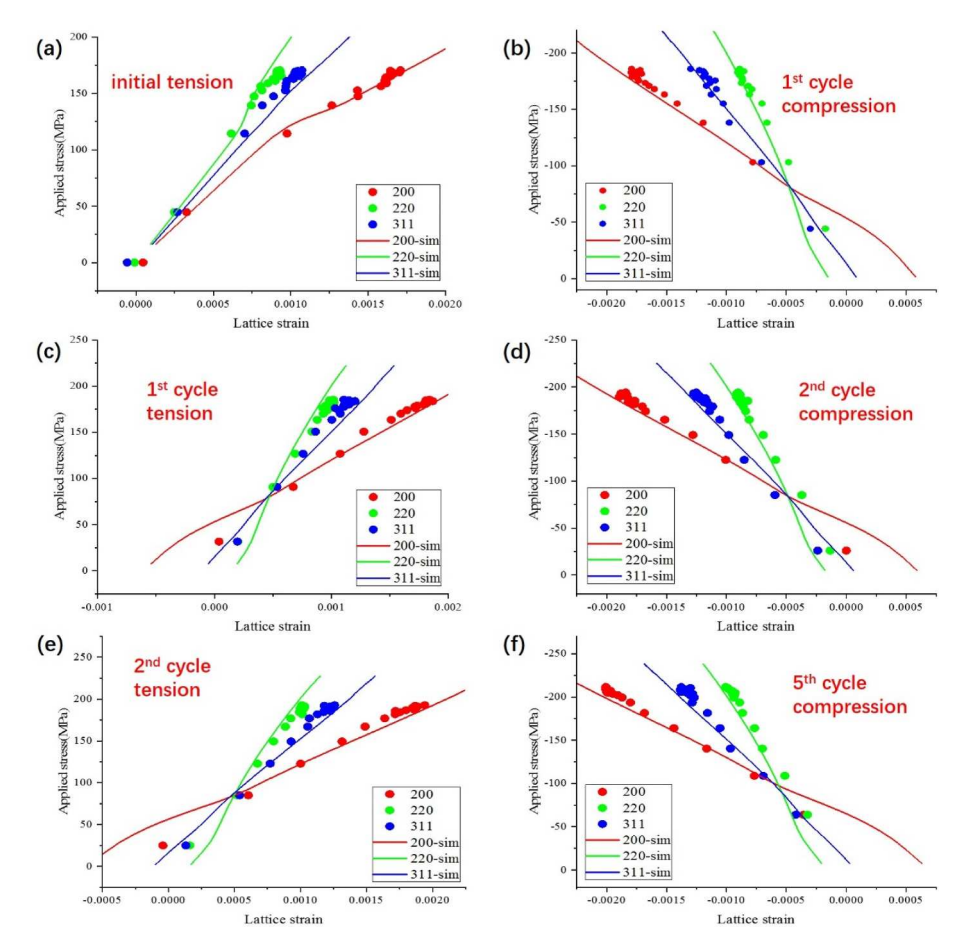


Fig. 9. Lattice-strain evolution with applied stress for specific grain families of the FCC Al_{0.3}CoCrFeNi HEA during (a) initial tension, (b) 1st cycle compression, (c) 1st cycle tension, (d) 2nd cycle compression, (e) 2nd cycle tension, and (f) 5th cycle compression.

their corresponding hardening parameters used in the Voce model in Eqs. (3) and (6) are listed in Table 1. Third, the above two steps will naturally give an excellent agreement with the stress-strain curves in the first loading stage, but the unloading and cyclic responses require the fitting to the backstress evolution in Eq. (7), where ξ and η are the governing constitutive parameters. Fitting to both lattice strain evolution in subsequent cycles (e.g., Fig. 9) and the overall stress-strain curves, results can be seen in Fig. 8 for these two alloys, illustrating the comparison between the mentioned two methods for specific cycles, where the initial tension and first ten cycles of simulated results are compared to the specific experiment data, i.e., initial tension, 1st, 2nd, 5th, and 10th cycles. Simulation results show good agreement with the

experiment data. With the increase of the number of cycles, the simulation results revealed the trend of the increasing stress amplitude. This result is consistent with the trend of the experiment and shows the cyclic-hardening effect of this alloy in the low-cycle number range. However, a similar phenomenon was observed in Al $_{0.5}$ CoCrFeNi under cyclic loading within the initial cycles [20], where rapid multiplication of dislocations existed. Another phenomenon should be noted is that the premature yielding behavior happens during the subsequent cycles after the initial tension. This result mainly correlates to the so-called Bauschinger effect, which results from the kinematic-hardening mechanism and has been found in Cantor alloy [50]. The existence of this effect causes a gentle rather than sharp change at the excessive position from

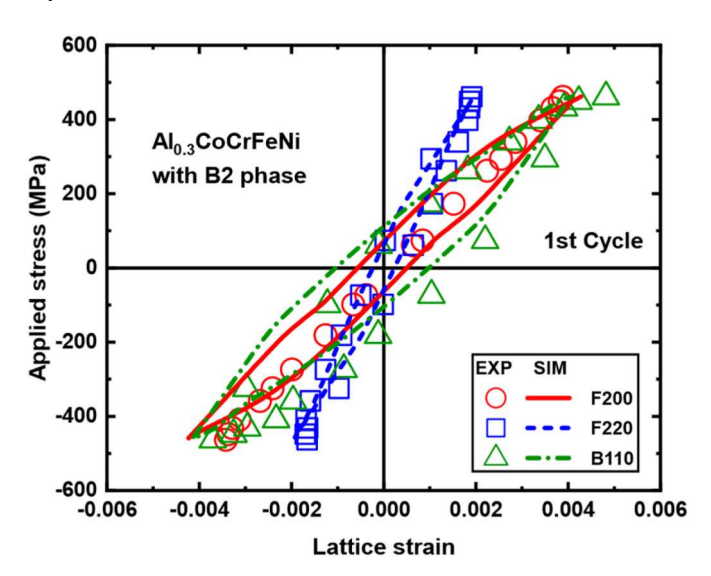


Fig. 10. Lattice-strain evolution with respect to the two-phase HEA of the first cycle, indicating the stronger B2 phase as shown from its {110} grain family.

Table 1Hardening parameters used in the EVPSC model. Parameters related to the back stress are included only for the cyclic-loading condition.

Sample	Phase	Hardening parameters (MPa)			Back Stress (MPa)		
		τ_0	τ_1	h ₀	h ₁	ξ	η
Al0.3-FCC Al0.3-FCC + B2	FCC FCC B2	62 71 321	20 57 26	40 62 47	0 44 33	3000 ≥11,000	110 127

 $\begin{tabular}{ll} \textbf{Table 2} \\ \textbf{Fitting parameters for the Basquin and Coffin-Manson laws in Fig. 3(b)}. \\ \end{tabular}$

Samples	σ_f (MPa)	$arepsilon_f^{'}$	b	c
Alo.3-FCC Alo.3-FCC + B2	193.4 3457.7	0.4310 8.5763	$-0.0226 \\ -0.1879$	$-0.4923 \\ -1.0042$

relaxation to reverse loading. Nevertheless, cyclic-loading curves of $Al_{0.3}$ CoCrFeNi showed strong tensile-compressive symmetry, where the stress level at the left lower corner was in the same range as that at the right upper corner. More discussions on ξ and η will be given shortly.

Fig. 9 illustrates the lattice strain versus applied uniaxial stress of {200}, {220}, and {311} grain families within the initial tension, 1st cycle compression and tension, 2nd cycle compression and tension, and 5th cycle compression along the loading direction, respectively. For the initial tension in Fig. 9(a), the lattice strain first increased linearly under ~ 123 MPa, where the material was under elastic deformation. However, {220}-oriented grains showed larger directional stiffness, as compared to the other two sets of grains. When the applied stress exceeded 123 MPa, the lattice strain will undergo obvious deflection, especially the {200}- and {220}-oriented grains, which indicates that the material has begun to undergo plastic deformation, and at the same time, the redistribution of the stress occurred between the grains of different orientations. Since the {220} grain family is softer, the deformation that can be accommodated within these grains was reduced, causing the lattice strain to deflect to the left. On the other hand, the {200} grain family accommodated more deformation with increasing their lattice distortion. During the 1st compression in Fig. 9(b), the lattice-strain evolution of the three specific crystal planes had the same discipline as the initial stretching stage, that is, the {220} grain family yielded first, and the {200} grain family accommodated more deformation under the same stress level. It is worth noting that the simulated

results show that there was a certain residual strain in the three orientation grains at a zero-stress level. Among them, the {200} grain family had a larger positive residual lattice strain of ~0.053%, which was caused by the accommodation of more deformations during the forward loading process but not the complete release during the reverse loading process. As for {220} and {311} grain families, they accommodated with less deformation, and the yielding occurred earlier with smaller accumulated lattice strains, which were almost completely released during the reverse loading process, resulting in relatively smaller residual lattice strains close to 0. Nevertheless, similar evolution exists within the following cycles, which can be observed in Fig. 9(c-f). It can be found that the redistribution of stress seems to be more inclined between the {220} and {200}, while the lattice strain of the {311}-oriented grains hardly undergo obvious deflection. Thus, it is foreseeable that during the entire cyclic-loading process, there is a stable and periodic stress redistribution and strain-release process between grains of different orientations in the Al0.3 with a single FCC phase.

Similar to the lattice strain evolution in Fig. 9, here we report the lattice strain evolution of the two phases in Fig. 10 for the first cycle. As indicated by the B2 $\{110\}$ grain family, during the initial tensile loading stage, the lattice strain shows rightward shifting, suggesting the higher strength of B2 phase (see Table 1). Successive cycles have already been shown in Fig. 8(b).

Back stresses are usually used to understand the dislocation behavior of metals and alloys under cyclic loading [51]. Dislocations will pile up against the interfaces to increase the plastic heterogeneity between different phases, which may lead to an increase in the back stress with the increasing cyclic numbers in low strain amplitudes [26]. The back stresses resulting from the dislocation accumulation of the incoherent precipitate could cause a lower LCF life. As shown in Eq. (7), the evolution of the back stress in a specific micro deformation system α mainly contains two terms (ξ and η) in the simulation. The ξ represents the linear kinematic hardening and the η is for the dynamic recovery. The fitting procedure has been discussed earlier in this section. As can be seen in Table 1, the value of ξ increases dramatically from 3000 MPa in the FCC sample to more than 11000 MPa in the FCC + B2 sample, while the η values are similar in the two samples. The effect of linear kinematic hardening term related to the coefficient ξ on back stress is dominant. This means that the introduction of the B2 precipitates mainly affects the kinematic hardening of α system in the matrix grains, while the effect on dynamic recovery is relatively weak. From the simulation results, the value of ξ increased due to the appearance of B2 phase, indicating that the B2 precipitate and its accompanying plastic heterogeneity indeed increased the overall back stress of the material, which is in good qualitative agreement with the TEM observations in Fig. 6(b). Therefore, the introduction of the B2 phase mainly increased the total back stress by affecting the kinematic hardening effect of the matrix grain slip system, and the increase in the back stress was the main reason for the decrease in the fatigue life of Al_{0.3}CoCrFeNi with B2 precipitates.

5. Conclusions

The B2 precipitates increased the yield strength and decreased the LCF life in the $Al_{0.3}$ CoCrFeNi HEA. The EVPSC model was used to simulate the LCF behavior of the $Al_{0.3}$ CoCrFeNi HEA based on the in-situ neutron diffraction measurements, which helped to understand the role of back stress in the LCF. The simulation results indicate that the B2 precipitates will increase the back stresses during cyclic loading by facilitating the kinematic hardening in the matrix, while the effect of dynamic recovery is relatively weak. This conclusion is supported by the direct TEM image showing the enhanced dislocation density near B2 precipitates. The lower LCF life of the $Al_{0.3}$ CoCrFeNi HEA with B2 precipitates was caused by the increase of back stress, which will provide more crack-initiation sites leading to a shorter fatigue life.

CRediT authorship contribution statement

Zongyang Lyu: Writing - review & editing, Writing - original draft, Visualization, Validation, Supervision, Software, Resources, Project administration, Methodology, Investigation, Formal analysis, Data curation, Conceptualization. Chuhao Liu: Writing - review & editing, Writing - original draft, Visualization, Validation, Supervision, Software, Resources, Project administration, Methodology, Investigation, Formal analysis, Data curation, Conceptualization. Di Xie: Writing review & editing, Writing - original draft, Visualization, Validation, Supervision, Software, Resources, Project administration, Methodology, Investigation, Formal analysis, Data curation, Conceptualization. Rui Feng: Writing - review & editing, Writing - original draft, Visualization, Validation, Supervision, Software, Resources, Project administration, Methodology, Investigation, Formal analysis, Data curation, Conceptualization. Dunji Yu: Writing - review & editing, Writing - original draft, Visualization, Validation, Supervision, Software, Resources, Project administration, Methodology, Investigation, Formal analysis, Data curation, Conceptualization. Yan Chen: Writing - review & editing, Writing - original draft, Visualization, Validation, Supervision, Software, Resources, Project administration, Methodology, Investigation, Formal analysis, Data curation, Conceptualization. Ke An: Writing review & editing, Writing - original draft, Visualization, Validation, Supervision, Software, Resources, Project administration, Methodology, Investigation, Formal analysis, Data curation, Conceptualization. Yanfei Gao: Writing - review & editing, Writing - original draft, Visualization, Validation, Supervision, Software, Resources, Project administration, Methodology, Investigation, Funding acquisition, Formal analysis, Data curation, Conceptualization. Huamiao Wang: Writing - review & editing, Writing – original draft, Visualization, Validation, Supervision, Software, Resources, Project administration, Methodology, Investigation, Funding acquisition, Formal analysis, Data curation, Conceptualization. Peter K. Liaw: Writing - review & editing, Writing - original draft, Visualization, Validation, Supervision, Software, Resources, Project administration, Methodology, Investigation, Funding acquisition, Formal analysis, Data curation, Conceptualization.

Declaration of competing interest

The authors declare no conflict of interest in this manuscript. The manuscript is approved by all authors for publication.

Data availability

Data will be made available on request.

Acknowledgments

The work was supported by the US National Science Foundation under DMR 1809640 to ZL, DX, PKL, and YG & under DMR 1611180 to ZL and PKL. ZL and DX also acknowledge the graduate fellowships from the Center for Materials Processing at the University of Tennessee. Neutron diffraction work was carried out at the Spallation Neutron Source (SNS), which is the U.S. Department of Energy (DOE) user facility at the Oak Ridge National Laboratory, sponsored by the Scientific User Facilities Division, Office of Basic Energy Sciences.

References

- [1] J.W. Yeh, S.K. Chen, S.J. Lin, J.Y. Gan, T.S. Chin, T.T. Shun, C.H. Tsau, S.Y. Chang, Nanostructured high-entropy alloys with multiple principal elements: novel alloy design concepts and outcomes, Adv. Eng. Mater. 6 (5) (2004) 299.
- [2] E.P. George, D. Raabe, R.O. Ritchie, High-Entropy Alloys Nature Rev. Mater. 4 (8) (2019) 515.
- [3] B. Cantor, I.T.H. Chang, P. Knight, A.J.B. Vincent, Microstructural development in equiatomic multicomponent alloys *Materials Science and Engineering: a* 375–377 (2004) 213.

- [4] Z. Li, K.G. Pradeep, Y. Deng, D. Raabe, C.C. Tasan, Metastable high-entropy dualphase alloys overcome the strength-ductility trade-off, Nature 534 (7606) (2016) 227.
- [5] Y.J. Liang, L. Wang, Y. Wen, B. Cheng, Q. Wu, T. Cao, Q. Xiao, Y. Xue, G. Sha, Y. Wang, Y. Ren, X. Li, L. Wang, F. Wang, H. Cai, High-content ductile coherent nanoprecipitates achieve ultrastrong high-entropy alloys, Nat. Commun. 9 (1) (2018) 4063.
- [6] Q. Ding, Y. Zhang, X. Chen, X. Fu, D. Chen, S. Chen, L. Gu, F. Wei, H. Bei, Y. Gao, M. Wen, J. Li, Z. Zhang, T. Zhu, R.O. Ritchie, Q. Yu, Tuning element distribution, structure and properties by composition in high-entropy alloys, Nature 574 (7777) (2019) 223.
- [7] Q. Ding, Y. Li, J. Ouyang, X. Wei, Z. Zhang, Y. Gao, H. Bei, The effect of stacking fault energy on the formation of nano twin/HCP during deformation in FCC concentrated solid solution (CSS) alloys *Materials Today Nano* 24 (2023) 100407.
- [8] Q. Pan, L. Zhang, R. Feng, Q. Lu, K. An, A.C. Chuang, J.D. Poplawsky, P.K. Liaw, L. Lu, Gradient cell–structured high-entropy alloy with exceptional strength and ductility, Science 374 (6570) (2021) 984.
- [9] P. Shi, R. Li, Y. Li, Y. Wen, Y. Zhong, W. Ren, Z. Shen, T. Zheng, J. Peng, X. Liang, P. Hu, N. Min, Y. Zhang, Y. Ren, P.K. Liaw, D. Raabe, Y.D. Wang, Hierarchical crack buffering triples ductility in eutectic herringbone high-entropy alloys, Science 373 (6557) (2021) 912.
- [10] Y. Lu, Y. Dong, S. Guo, L. Jiang, H. Kang, T. Wang, B. Wen, Z. Wang, J. Jie, Z. Cao, H. Ruan, T. Li, A promising new class of high-temperature alloys: eutectic high-entropy alloys, Sci. Rep. 4 (2014) 6200.
- [11] M. Wu, I. Baker, High strength and high ductility in a novel Fe40.2Ni11.3Mn30Al7.5Cr11 multiphase high entropy alloy, J. Alloys Compd. 820 (2020) 153181.
- [12] D.B. Miracle, O.N. Senkov, A critical review of high entropy alloys and related concepts, Acta Mater. 122 (2017) 448.
- [13] Z. Wu, Y. Gao, H. Bei, Thermal activation mechasnims and Labusch-type strengthening analysis for a family of high-entropy and equiatomic solid-solution alloys, Acta Mater. 120 (2016) 108–119.
- [14] S.A.A. Shams, G. Jang, J.W. Won, J.W. Bae, H. Jin, H.S. Kim, C.S. Lee, Low-cycle fatigue properties of CoCrFeMnNi high-entropy alloy compared with its conventional counterparts *Materials Science and Engineering: a* 792 (2020) 139661.
- [15] S.A.A. Shams, G. Kim, J.W. Won, J.N. Kim, H.S. Kim, C.S. Lee, Effect of grain size on the low-cycle fatigue behavior of carbon-containing high-entropy alloys *Materials Science and Engineering: a* 810 (2021) 140985.
- [16] K. Lu, A. Chauhan, A.S. Tirunilai, J. Freudenberger, A. Kauffmann, M. Heilmaier, J. Aktaa, Deformation mechanisms of CoCrFeMnNi high-entropy alloy under low-cycle-fatigue loading, Acta Mater. 215 (2021) 117089.
- [17] Z. Zhang, X. Zhai, G. Chen, X. Chen, K. Ameyama, Enhanced synergy of strength-ductility and low-cycle fatigue resistance of high-entropy alloy through harmonic structure design. Scripta Mater. 213 (2022) 114591.
- [18] L. Xu, Y. Jia, S. Wu, Y. Mu, Y. Jia, G. Wang, Low Cycle Fatigue Properties of Refractory High-Entropy HfNbTiZr Alloy *Intermetallics*, vol. 152, 2023 107751.
- [19] A. Radi, S. Sajadifar, S.V. Seyedmohammadi, M. Krochmal, A. Bolender, T. Wegener, T. Niendorf, G.G. Yapici, On the low-cycle fatigue behavior of a multiphase high entropy alloy with enhanced plasticity, Int. J. Fatig. 173 (2023) 107678
- [20] R. Feng, Y. Rao, C. Liu, X. Xie, D. Yu, Y. Chen, M. Ghazisaeidi, T. Ungar, H. Wang, K. An, P.K. Liaw, Enhancing fatigue life by ductile-transformable multicomponent B2 precipitates in a high-entropy alloy, Nat. Commun. 12 (1) (2021) 3588.
- [21] K. Lu, F. Knöpfle, A. Chauhan, H.T. Jeong, D. Litvinov, M. Walter, W.J. Kim, J. Aktaa, Low-cycle fatigue behavior and deformation mechanisms of a dual-phase Al0.5CoCrFeMnNi high-entropy alloy, Int. J. Fatig. 163 (2022) 107075.
- [22] S.A.A. Shams, J.W. Bae, J.N. Kim, H.S. Kim, T. Lee, C.S. Lee, Origin of superior low-cycle fatigue resistance of an interstitial metastable high-entropy alloy, J. Mater. Sci. Technol. 115 (2022) 115.
- [23] S.A.A. Shams, G. Jang, J.W. Bae, A. Amanov, H.S. Kim, T. Lee, C.S. Lee, Low-cycle Fatigue Behavior and Surface Treatment of a Twinning-Induced Plasticity High-Entropy Alloy Materials Science and Engineering: A., vol. 853, 2022 143724.
- [24] S.A.A. Shams, G. Kim, C.S. Lee, H.S. Kim, H.R. Jafarian, The Astonishing Effect of Si Addition on Low-Cycle Fatigue Life in a Metastable High-Entropy Alloy Materials Science and Engineering: A., vol. 880, 2023 144985.
- [25] K. Hockauf, M.F.X. Wagner, T. Halle, T. Niendorf, M. Hockauf, T. Lampke, Influence of precipitates on low-cycle fatigue and crack growth behavior in an ultrafine-grained aluminum alloy, Acta Mater. 80 (2014) 250.
- [26] H. Xu, D. Ye, L. Mei, A Study of the Back Stress and the Friction Stress Behaviors of Ti-6Al-4V Alloy during Low Cycle Fatigue at Room Temperature Materials Science and Engineering: A., vol. 700, 2017, p. 530.
- [27] X.L. Wang, T.M. Holden, G.Q. Rennich, A.D. Stoica, P.K. Liaw, H. Choo, C. R. Hubbard, VULCAN—the engineering diffractometer at the SNS, Phys. B Condens. Matter 385–386 (2006) 673.
- [28] K. An, H.D. Skorpenske, A.D. Stoica, D. Ma, X.-L. Wang, E. Cakmak, First in situ lattice strains measurements under load at VULCAN, Metall. Mater. Trans. 42 (1) (2010) 95.
- [29] K. An, VDRIVE-data Reduction and Interactive Visualization Software for Event Mode Neutron Diffraction ORNL Report, Oak Ridge National Laboratory, 2012. ORNL-TM-2012-621.
- [30] H. Wang, P.D. Wu, C.N. Tomé, Y. Huang, A finite strain elastic-viscoplastic self-consistent model for polycrystalline materials, J. Mech. Phys. Solid. 58 (4) (2010) 594.
- [31] A.S. Tirunilai, T. Hanemann, C. Reinhart, V. Tschan, K.P. Weiss, G. Laplanche, J. Freudenberger, M. Heilmaier, A. Kauffmann, Comparison of Cryogenic

- Deformation of the Concentrated Solid Solutions CoCrFeMnNi, CoCrNi and CoNi Materials Science and Engineering: A., vol. 783, 2020 139290.
- [32] H.Y. Yasuda, K. Shigeno, T. Nagase, Dynamic strain aging of Al 0.3 CoCrFeNi high entropy alloy single crystals, Scripta Mater. 108 (2015) 80.
- [33] W. Wei, Y. Feng, L. Han, Q. Zhang, J. Zhang, Cyclic Hardening and Dynamic Strain Aging during Low-Cycle Fatigue of Cr-Mo Tempered Martensitic Steel at Elevated Temperatures Materials Science and Engineering: A., vol. 734, 2018, p. 20.
- [34] V. Shankar, A. Kumar, K. Mariappan, R. Sandhya, K. Laha, A.K. Bhaduri, N. Narasaiah, Occurrence of dynamic strain aging in Alloy 617M under low cycle fatigue loading, Int. J. Fatig. 100 (2017) 12.
- [35] Y.-H. Lin, K.-H. Hu, F.-H. Kao, S.-H. Wang, J.-R. Yang, C.-K. Lin, Dynamic Strain Aging in Low Cycle Fatigue of Duplex Titanium Alloys Materials Science and Engineering: A., vol. 528, 2011, p. 4381, 13-14.
- [36] H. Zhou, Y. He, H. Zhang, Y. Cen, Influence of dynamic strain aging pre-treatment on the low-cycle fatigue behavior of modified 9Cr-1Mo steel, Int. J. Fatig. 47 (2013) 83
- [37] K. Lu, A. Chauhan, D. Litvinov, M. Walter, A.S. Tirunilai, J. Freudenberger, A. Kauffmann, M. Heilmaier, J. Aktaa, High-temperature Low Cycle Fatigue Behavior of an Equiatomic CoCrFeMnNi High-Entropy Alloy Materials Science and Engineering: A., vol. 791, 2020 139781.
- [38] G. Sudhakar Rao, J.K. Chakravartty, N. Saibaba, G.S. Mahobia, K. Chattopadhyay, N.C. Santhi Srinivas, V. Singh, Disappearance and Reappearance of Serrated Plastic Flow under Cyclic Loading: A Study of Dislocation Substructures Materials Science and Engineering: A., vol. 603, 2014, p. 114.
- [39] S. Hong, K. Lee, S. Lee, Dynamic strain aging effect on the fatigue resistance of type 316L stainless steel, Int. J. Fatig. 27 (10–12) (2005) 1420.
- [40] H.G. Lambers, C.J. Rüsing, T. Niendorf, D. Geissler, J. Freudenberger, H.J. Maier, On the low-cycle fatigue response of pre-strained austenitic Fe61Mn24Ni6.5Cr8.5 alloy showing TWIP effect, Int. J. Fatig. 40 (2012) 51.

- [41] S. Nandy, A.P. Sekhar, T. Kar, K.K. Ray, D. Das, Influence of ageing on the low cycle fatigue behaviour of an Al-Mg-Si alloy, Phil. Mag. 97 (23) (2017) 1978.
- [42] J. Jadav, K.V. Rajulapati, K.B.S. Rao, N.E. Prasad, R. Mythili, K. Prasad, Strain Controlled Isothermal Low Cycle Fatigue Life, Deformation and Fracture Characteristics of Superni 263 Superalloy Materials Science and Engineering: A., vol. 760, 2019, p. 296.
- [43] O. Basquin, The exponential law of endurance tests, Proc. Am. Soc. Test Mater. 10 (1910) 625.
- [44] S.S. Manson, Behavior of Materials under Conditions of Thermal Stress National Advisory Committee for Aeronautics, 1953. Technical Report 2922.
- [45] L.F. Coffin Jr., A study of the effects of cyclic thermal stresses on a ductile metal, Trans. Am. Soc. Mech. Eng. 76 (6) (1954) 931.
- [46] S. Huang, D.W. Brown, B. Clausen, Z. Teng, Y. Gao, P.K. Liaw, In Situ Neutron-Diffraction Studies on the Creep Behavior of a Ferritic Superalloy Metallurgical and Materials Transactions A, vol. 43, 2011, p. 1497, 5.
- [47] S. Huang, Y. Gao, K. An, L. Zheng, W. Wu, Z. Teng, P.K. Liaw, Deformation mechanisms in a precipitation-strengthened ferritic superalloy revealed by in situ neutron diffraction studies at elevated temperatures, Acta Mater. 83 (2015) 137.
- [48] D. Yu, K. An, Y. Chen, X. Chen, Revealing the Cyclic Hardening Mechanism of an Austenitic Stainless Steel by Real-Time in Situ Neutron Diffraction Scripta Materialia, vol. 89, 2014, p. 45.
- [49] D. Xie, Z. Lyu, M. Fan, H.B. Chew, P.K. Liaw, H. Bei, Z. Zhang, Y. Gao, Micromechanical Origin of the Enhanced Ductility in Twinless Duplex Mg–Li Alloy Materials Science and Engineering: A., vol. 815, 2021 141305.
- [50] O. Bouaziz, J. Moon, H.S. Kim, Y. Estrin, Isotropic and kinematic hardening of a high entropy alloy, Scripta Mater. 191 (2021) 107.
- [51] G. Sudhakar Rao, J.K. Chakravartty, S. Nudurupati, G.S. Mahobia, K. Chattopadhyay, N.C. Santhi Srinivas, V. Singh, Low cycle fatigue behavior of Zircaloy-2 at room temperature, J. Nucl. Mater. 441 (1–3) (2013) 455.